

Nanoscale

Accepted Manuscript



This is an *Accepted Manuscript*, which has been through the Royal Society of Chemistry peer review process and has been accepted for publication.

Accepted Manuscripts are published online shortly after acceptance, before technical editing, formatting and proof reading. Using this free service, authors can make their results available to the community, in citable form, before we publish the edited article. We will replace this *Accepted Manuscript* with the edited and formatted *Advance Article* as soon as it is available.

You can find more information about *Accepted Manuscripts* in the [Information for Authors](#).

Please note that technical editing may introduce minor changes to the text and/or graphics, which may alter content. The journal's standard [Terms & Conditions](#) and the [Ethical guidelines](#) still apply. In no event shall the Royal Society of Chemistry be held responsible for any errors or omissions in this *Accepted Manuscript* or any consequences arising from the use of any information it contains.



Reduced graphene oxide nanofiltration membrane intercalated by well-dispersed carbon nanotubes for drinking water purification

Xianfu Chen, Minghui Qiu, Hao Ding, Kaiyun Fu and Yiqun Fan*

Received 00th January 20xx,
Accepted 00th January 20xx

DOI: 10.1039/x0xx00000x

www.rsc.org/

In this study, we report a promising rGO-CNTs hybrid nanofiltration (NF) membrane that was fabricated by loading reduced graphene oxide that were intercalated with carbon nanotubes (rGO-CNTs) onto an anodic aluminum oxide (AAO) microfiltration membrane via a facile vacuum-assisted filtration process. To create this NF membrane, CNTs were first dispersed using block copolymers (BCPs); the effects of the types and contents of BCPs used on the dispersion of CNTs have been investigated. The as-prepared rGO-CNTs hybrid NF membranes were then used for drinking water purification to retain the nanoparticles, dyes, protein, organophosphate, sugars, and particularly humic acid. Experimentally, it is shown that the rGO-CNTs hybrid NF membranes have a high retention efficiency, good permeability and good anti-fouling properties. The retention was above 97.3% even for methyl orange (327 Da); for other objects, the retention was above 99%. The membrane's permeability was found to be as high as 20–30 L·m⁻²·h⁻¹·bar⁻¹. Based on these results, we can conclude that i) the use of BCPs as a surfactant can enhance steric repulsion and thus disperse CNTs effectively; ii) placing well-dispersed 1D CNTs within 2D graphene sheets allows a uniform network to form, which can provide many mass transfer channels through the continuous 3D nanostructure, resulting in a high permeability and separation performance of the rGO-CNTs hybrid NF membranes.

Introduction

Water crises represent the highest impact of all risks, even above those of weapons of mass destruction, interstate conflict and the spread of infectious diseases (pandemics), as reported in the 2015 Global Risks Report from the World Economic Forum.¹ Membranes have been used widely in water treatment and purification due to their low-cost, high-efficiency and environmentally friendly characteristics. Nanofiltration (NF), which ranges between ultrafiltration (UF) and reverse osmosis (RO), is a type of pressure-driven membrane process that is used to selectively separate solutes with molecular weights ranging from 200 to 1000 Da from a solvent-solute mixture.² This method is generally more effective at separating small molecular substances than UF and can produce high-quality drinking water at much lower capital and operating costs compared to RO.^{3,4} Particularly, NF has excellent characteristics in selectively removing ions due to several exclusion forces that exist at the interfaces between the NF material and the solution, including steric exclusion, Donnan equilibrium and potentially dielectric exclusion.^{5–8} This advantage of NF allow it to hold specific ions that are beneficial to the human body, while removing harmful materials such as fluoride, arsenic and other

hazardous ions.^{9–11} For these reasons, NF has attracted extensive attention towards the treatment of drinking water using NF membranes in recent years.^{9, 12–14}

Both organic and inorganic NF membranes can be fabricated and applied to drinking water purification and wastewater treatment. A promising membrane should provide high flux and selectivity, improved stability, and superior resistance to acid-base and special solvents.¹⁵ Additionally, this membrane should offer both an initially high permeation flux and a high resistance to fouling during operation. Currently, extensive studies have been focused on the fabrication of high performance membranes with isoporous structure,¹⁶ fast water channels,¹⁷ hydrophilic surfaces¹⁸ and other special properties¹⁹ to increase permeability and anti-fouling.

As a new type of 2D nano materials, graphene and its derivatives have been commonly used in the fabrication of effective separation membranes due to their chemical and mechanical stability, structural flexibility and, most importantly, single-atom thickness.^{20–26} In recent years, many theoretical and experimental studies have shown that graphene-based materials could be applied to produce a highly selective and permeable separation membrane with higher performance in water purification than state-of-the-art polymer-based or even inorganic filtration membranes.^{27–29}

However, due to the narrow interlayer spacing (< 0.8 nm), most graphene-based membranes with high permeation flux were obtained by reducing their thickness as much as possible (< 50 nm). Remarkably, tuning the interlayer spacing of graphene-based materials with nano-sized materials has become an alternative solution to improving the permeability

State Key Laboratory of Materials-Oriented Chemical Engineering, College of Chemical Engineering, Nanjing Tech University, Nanjing, 210009, P. R. China. E-mail: yiqunfan@njtech.edu.cn; Tel.: +86 25 83172277; Fax: +86 25 83172292.

† Electronic Supplementary Information (ESI) available. See DOI: 10.1039/x0xx00000x

of these filters. These nano-sized materials could be small organic molecules,³⁰⁻³² inorganic nano particles,^{33, 34} or nano tubes/fibers.^{21, 35-37} Among them, carbon nanotubes (CNTs) are the most promising due to their extraordinary mechanical, electrical, thermal, optical, chemical properties and, most importantly, their compatibility with graphene-based materials.³⁸ Unfortunately, the poor dispersion and stabilization of CNTs in solvent media, particularly in water, markedly limit their applications. To address this issue, many studies have attempted to develop effective dispersing agents for CNTs.³⁹⁻⁴³ Among the available dispersing agents, block copolymers (BCPs) show good potential for the dispersion of CNTs, particularly in water.⁴⁰⁻⁴³ However, few studies in the literature have investigated the effect of CNTs dispersion on the properties of graphene-based membranes that have been intercalated by CNTs.

In this study, we create rGO-CNTs hybrid NF membranes with high permeability by adjusting their interlayer spacings with CNTs. We systematically study CNTs dispersion in water using commercially available BCPs as the dispersing agent and the performance of graphene NF membranes for water purification in terms of the permeability and the retention for nanoparticles, proteins, dyes, sugars, and, particularly humic acid.

Experimental

2.1. Dispersion of CNTs.

A total of 2 mg of multi-walled carbon nanotubes (CNTs) were added to 100 mL of block copolymers (BCPs) in water with an arranged weight percent. Then, a small amount of alcohol was added. The BCPs-CNTs suspension was then subjected to horn sonication at 500 W in an ice bath for 10 min to disperse the CNTs completely and then form a series of stable composite dispersions. All chemicals were purchased from Sigma-Aldrich and used as received.

2.2. Preparation of rGO dispersions.

The procedure of the GO chemical reduction was similar to that described in the literature,⁴⁴ and the details are described below. In the beginning, 1.4 mmol of L-ascorbic acid (a form of vitamin) was added to 25 mL GO dispersion (0.02 mg/mL). Then, 20 μ L of ammonia solution (25 wt.%) was added to adjust the pH of the mixture. The mixture was then vigorously shaken for several times and then stirred at 95 °C for 30 min. The mixture was then cooled to room temperature to obtain the reduced GO (rGO) dispersion. All chemicals were purchased from Sigma-Aldrich and used as received.

2.3. Preparation of CNTs intercalated graphene membranes.

The as-prepared CNTs dispersion (0.02 mg·mL⁻¹) and rGO dispersion (0.02 mg·mL⁻¹) were mixed at a ratio of 1:2 by volume to form a rGO-CNTs "solution" using sonication for 10 min at 500 W in an ice bath. Anodic aluminum oxide (AAO) macroporous membranes with an average pore size of 100 nm and a thickness of 50 μ m from Whatman Ltd (Germany) were used as substrates for rGO-CNTs hybrid membranes. rGO-CNTs hybrid membranes were prepared on the enhanced AAO

substrates via a vacuum-assisted filter method at room temperature. The pressure at vacuum side was controlled below 100 Pa. The thickness of the membrane was controlled by adjusting the volume of the added CNT-rGO dispersion. The vacuum conditions were held constant for two additional hours until no liquid could be observed on the surface of fresh membrane to remove most of the water in the rGO-CNTs hybrid membrane. The as-prepared fresh rGO-CNTs hybrid membranes were dried at 70 °C for 12 h to remove the residual water. The appearance of the obtained rGO-CNTs hybrid membrane is shown in Fig. S1. Both the AAO disk and rGO-CNTs hybrid membrane were so thin. We could easily distinguish the characters behind them by naked eyes.

2.4. Characterization.

Fourier transform infrared (FTIR) spectra of GO/rGO were measured using a Nicolet 8700 infrared microspectrometer (Thermo, USA) in the range of 4000-1000 cm⁻¹. Raman spectra (LabRAM HR 800, Horiba, France) were recorded using an excitation wavelength of 514 nm (2.41 eV). An X-ray diffractometer (XRD) (Miniflex 600, Rigaku, Japan) was used to measure the interlayer with focused monochromatized Cu-K α radiation at a wavelength of 1.5418 Å operating in the 2 θ range of 5-50° at a scan rate of 20°·min⁻¹. The average d-spacing value was calculated using Bragg's law from the X-ray scattering data. The particle size distribution of the sample was characterized by dynamic light scattering (DLS, Microtrac, Zetatract, USA). FESEM (S-4800, Hitachi, Japan), TEM (1011, JEOL, Japan) and AFM (XE-100, Park, Korea) were used to characterize the microtopographies of the samples. The strength and scratch resistance of the membranes were measured using a nano-scratch tester (NanoTest, MML, England).

To understand the performance of the rGO-CNTs hybrid NF membranes, the pure-water permeability and the retention of Au nanoparticles ($d_m=2$ nm), BSA, dyes, phoxim, sugars, humic acid and ions were measured at room temperature in a dead-end stirred cell filtration system (Millipore, Micron 8010, USA). The retention of the rGO-CNTs hybrid membranes were determined by measuring the concentrations of both the feed and the permeate side, and were calculated using equation (1):

$$R(\%) = (1 - C_p/C_f) \times 100 \quad (1)$$

where R is the retention of the membrane, C_p is the concentration of the permeate solution and C_f is the concentration of the feed solution. The concentrations of Au nanoparticles, BSA, dyes, and humic acids were identified by UV-vis spectrophotometer (Thermo, Nanodrop 2000, USA). The concentrations of phoxim and various sugars were identified by an HPLC system (Agilent, 1100 Series, USA) and a GPC system (Waters, 1515, USA), respectively. The concentrations of ions were tested by using inductively-coupled plasma spectrometer (Bruker, Autoflex speed, Germany). Based on the retention curve for various sugars, the molecular weight cut-off (MWCO) of the NF membrane was obtained. The relationship between the molecular stocks radius and molecular weight was calculated using equation (2)⁴⁵:

$$r = 0.262 \times (M_w)^{0.5} - 0.3, \quad (2)$$

where r is the molecular stocks radius (Å), and M_w is the molecular weight (Da).

3 Results and Discussion

3.1. Dispersion of CNTs.

The CNTs exhibited an average diameter of 6-10 nm and an average length of 1-12 μm . The CNTs tended to become intertwined like balls of loose twine (Fig. S2a-b) due to their high L/D ratio. As a result, the CNTs were not well dispersed in water or ethanol even in the presence of general surfactants, such as sodium dodecyl benzene sulfonate (SDBS). Even after a high level of SDBS was added (i.e., mass ratio of SDBS: CNTs reached as high as 10: 1), there were still many particles that could be observed by naked eyes (Fig. S2c). Conversely, the CNTs are well dispersed in the case of using block copolymers (BCPs) as a dispersing agent, even with a small amount added.

The effect of BCP addition on the CNTs microstructures was evaluated using TEM (Fig. S3). Without the BCPs, the CNTs intertwine tightly, making it hard to distinguish them because their outside walls are smooth. Conversely, with the addition of BCPs, the boundary of the CNTs' outside walls begun to blur, while the intertwining effect between the CNTs weakened due to the steric inhibition of BCPs.

The Pluronic® types are block copolymers based on ethylene oxide and propylene oxide. Two commercially available linear PEO-PPO-PEO triblock copolymers of the Pluronic® series, F127

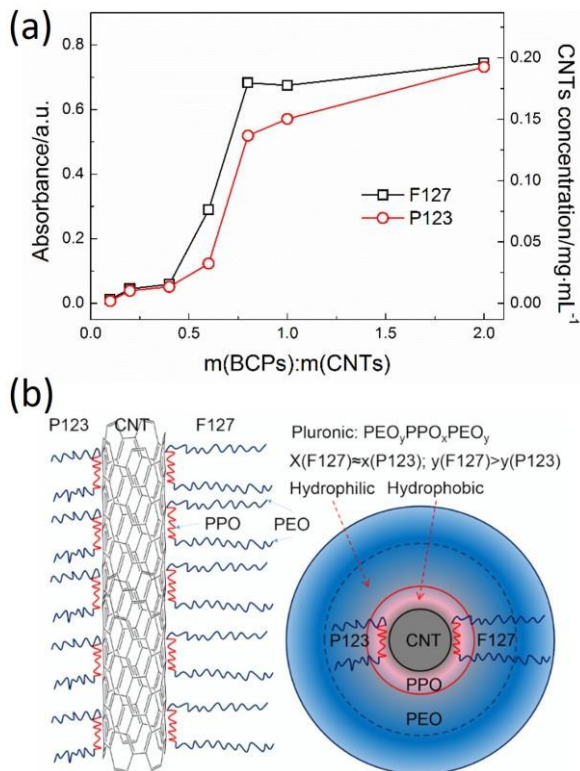


Fig. 1 (a) Effect of the amount of BCPs added on CNTs dispersion. (b) Proposed mechanism of BCPs on CNTs dispersion, and the difference between P123 and F127.

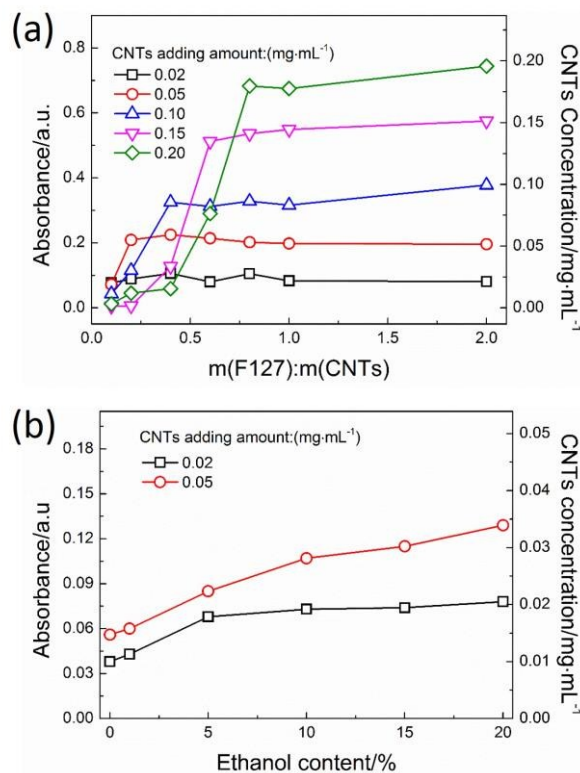


Fig. 2 (a) Effects of the amount of F127 added on CNTs dispersion at various concentrations. (b) Effect of ethanol content on CNTs dispersion.

and P123 in the dispersion of the CNTs were used and were evaluated via Uv-vis absorption analysis at a wavelength of 350 nm, respectively.^{41, 46} Fig. 1a, F127 shows an enhanced capacity for the dispersion of CNTs. At the mass ratio $m(\text{BCPs}) : m(\text{CNTs})$ of 0.8, the concentration of the dispersed CNTs in the dispersion is approximately 0.19 $\text{mg}\cdot\text{mL}^{-1}$, which is near the initial amount (0.2 $\text{mg}\cdot\text{mL}^{-1}$) of CNTs added, when using F127 as the dispersing agent. Conversely, the dispersed CNTs concentration in the dispersion when using P123 was only approximately 0.14 $\text{mg}\cdot\text{mL}^{-1}$.

The particle size distribution of CNTs was characterized as DLS. As shown in Fig. S4, the CNTs dispersed by F127 show a narrow unimodal distribution with an average particle size of approximately 150 nm, while that dispersed by P123 show a wider particle size distribution. Note that the particle size distribution determined by DLS in this study and below are a qualitative analysis rather than a quantitative analysis due to the nature of the CNTs' 1D structure.

It has been well demonstrated that PEO-PPO-PEO triblock copolymers significantly inhibit nanotube aggregation primarily via steric repulsion. When mixing with CNTs, the PO groups anchor the sidewall of the CNTs, while the EO groups extend into the water to create steric repulsion.⁴⁰ A possible mechanism for CNTs dispersion by BCPs and the behavioral difference between P123 and F127 are shown in Fig. 1b. F127 shows a longer PEO block (2×106 EO units) than P123 (2×20 EO units), indicating that F127 is more hydrophilic than P123.^{47, 48} Thus, the use of F127 can produce a relatively thicker

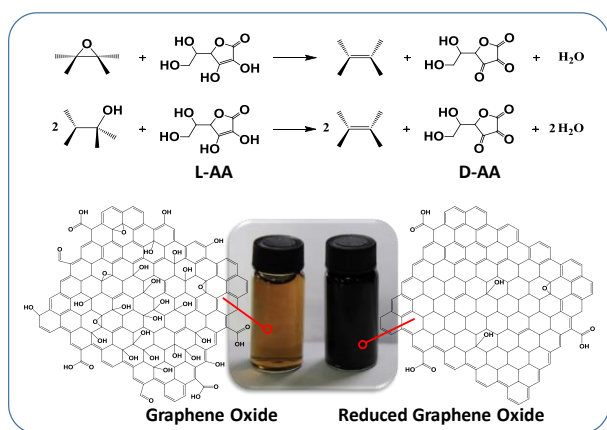


Fig. 3 Schematic illustration of the proposed reaction pathway of GO by L-AA.

hydration shell, leading to an enhanced steric repulsion. As a result, F127 exhibits a higher capacity to disperse CNTs than P123. Therefore, it was selected as the dispersing agent in the following studies.

The effects of the F127 content on the dispersion of CNTs at various concentrations are shown in Fig. 2a. Both the absorbance and the dispersed CNTs concentration first increase and then approach a maximum as F127 content increases. In addition, critical F127 contents for the well-dispersed CNTs at various concentrations from 0.02 to 0.2 mg·mL⁻¹ are shown. The critical amount of the dispersant is shown to increase with the initial amount of CNTs added. As a result, the initial CNTs content should not be too high (< 0.1 mg·mL⁻¹) to reduce the required surfactant content.

The particle size distribution of the fresh CNTs dispersant when the initial CNTs content is 0.02 mg·mL⁻¹, which corresponds to the critical F127 ratio of 0.1, shows a narrow unimodal distribution with an average particle size of

approximately 150 nm. Conversely, the dispersion shows a wide particle size distribution, which can be attributed to a marginal aggregation of CNTs due to the two-week storage duration this sample experienced. To re-disperse the CNTs agglomeration, we performed an ultrasonic treatment again. The particle size distribution of re-dispersed CNTs was found to be nearly identical to that of the fresh sample (Fig. S5a). Therefore, it is suggested that fresh F127 be used or that the mixture is retreated using ultrasound to obtain good dispersion performance. Additionally, the particle size distribution after CNTs dispersion with F127 after two weeks of storage without ultrasound retreatment at different F127 contents is shown in Fig S4b. The dispersion shows a wide particle size distribution when the mass ratio $m(\text{F127}): m(\text{CNTs})$ is below 0.4 and a good unimodal distribution when that ratio is higher than 0.4.

To further increase the CNTs dispersion and reduce the F127 content, ethanol was applied as a second solvent during CNTs dispersion. As shown in Fig. 2b, the alcohol content reduced the amount of F127 to half of the critical value in pure water. The mass ratios $m(\text{F127}): m(\text{CNTs})$ were 0.05 and 0.1 for CNTs dispersion with the total amounts added equal to 0.02 and 0.05 mg·mL⁻¹, respectively; the addition of ethanol could thus promote CNTs dispersion, and ethanol is a good solution to reduce F127 content, which could provide better solvent conditions for F127.⁴⁹ As a result, the entropic repulsion among the tethered chains generates a free energy barrier to prevent CNTs from approaching the attractive part of intertube potential.⁴⁶ When the ethanol content was 5-10 wt.%, the CNTs were well dispersed with a lower amount of F127, of which the dispersed concentration was near the initial amount that was added. However, a large amount of CNTs did not disperse well even at higher ethanol contents (e.g., 20%). The above results indicate that the effect of the addition of F127 on CNTs dispersion is strong, but that of the ethanol is small. Therefore,

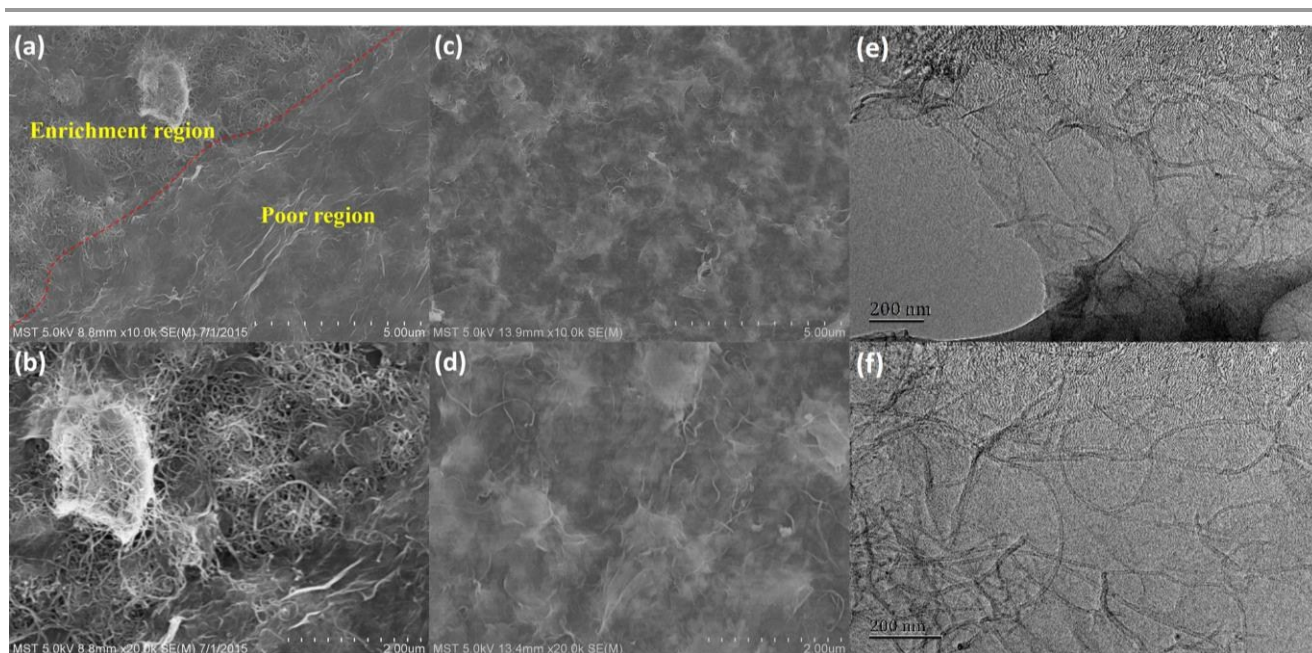


Fig. 4 FESEM images of rGO-CNTs hybrid NF membranes. (a,b) poor dispersion; (c,d) well dispersion. (e,f) TEM images of rGO-CNTs hybrid NF membrane.

Table 1 Effect of CNT dispersion on the permeability and retention properties of rGO-CNTs membranes

Sample	Mw/Da	Poor dispersion		Well dispersion	
		J/L·m ⁻² ·h ⁻¹ ·bar ⁻¹	R/%	J/L·m ⁻² ·h ⁻¹ ·bar ⁻¹	R/%
Pure water	18	66.5	---	31.5	---
Direct Red 80	1373	52.3	48.1	26.4	>99
Chlorazol Fast Pink	991	55.6	48.3	27.7	>99
Chlorazol Black	782	58.2	46.2	26.1	>99
Titan Yellow	696	57.6	44.4	25.9	>99
Methyl Orange	327	61.2	27.5	29.1	97.3

the initial CNTs content was chosen as 0.02 mg·mL⁻¹, the mass ratio m(F127): m(CNTs) was optimised to 0.05, and the ethanol content was controlled at 10 wt.% to obtain well-dispersed CNTs in the following studies.

3.2. Chemically reduced GO

Graphene oxide was reduced with L-AA in a water bath. A schematic illustration of the proposed reaction pathway⁴⁴ is shown in Fig. 3. The C-O-C and -OH groups that existed on the sheets of graphene oxide were reduced to C=C groups by L-AA, and the L-AA was oxidized into D-AA. After reduction, the slurry turned from brown to black in color due to the loss of oxygen-containing functional groups. Additionally, the reduced GO sheets dispersed well in water, which is likely caused by the fact that the reducing agent L-AA could shell the edges of the reduced GO sheets and prevent the aggregation of these sheets from forming precipitates. An AFM image of reduced GO sheet on mica is shown in Fig. S6. The reduced GO sheet, which had an average size of approximately 2 μm and is flattened on the mica substrate, concurrently exhibits defect holes.

FTIR, XRD and Raman spectra of GO and reduced GO (rGO) are shown in Fig. S7a-c, respectively. For GO, many hydrophilic functional groups that have excellent water-absorbing capacities were observed. Two peaks were observed near 3430 cm⁻¹ and 1635 cm⁻¹ are known to refer to the -OH groups of absorbed water in GO, while the peaks at 2930 cm⁻¹ and 2850 cm⁻¹ refer to the -CH₂- groups on the GO sheets. The peak at 1720 cm⁻¹ can be attributed to the C=O stretching vibrations of carbonyl or conjugated carbonyl groups. The peaks at 1380 cm⁻¹, 1264 cm⁻¹ and 1110 cm⁻¹ likely indicate the -OH groups of carboxyl, C-O-C groups of epoxy ether, and C-O groups of alkoxy, respectively. Conversely, the peaks of the -OH and C-O-C groups nearly disappear with respect to the reduced GO. However, there are still strong indications of the existence of C=O groups in the reduced GO sheets. Fig. S7b shows that the 2-theta degree of the sharp peak with reference to the reduced GO is larger than that of the GO; this is because the loss of functional groups in the reduction process will decrease the d-spacing of the graphene sheets. Based on the Bragg equation,⁵⁰ the d-spacings were calculated to be 0.521 nm and 0.885 nm for

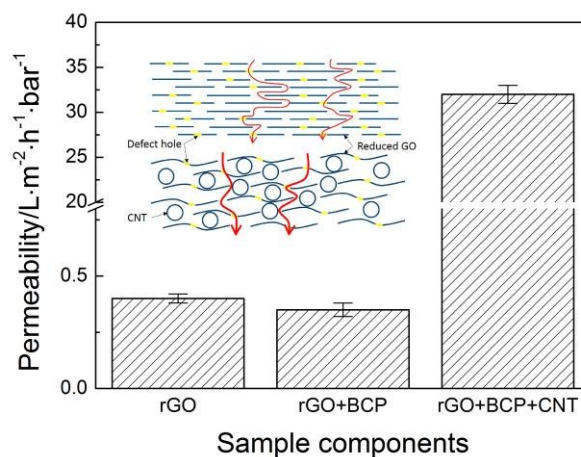


Fig. 5 Pure water permeabilities of various membranes with different components and proposed effect of CNTs on the structure of graphene membrane (inset).

reduced GO and GO, respectively. From the Raman spectrum (Fig. S7c), typical D and G bands could be found at approximately 1355 and 1575 cm⁻¹, respectively. The G band is a doubly degenerate phonon mode at the Brillouin zone center, which represents the sp² carbon networks. Conversely, the D band is a breathing mode of six-atom rings and requires the existence of defects for activation. After chemical reduction, a higher Raman D/G peak height ratio can be observed for the reduced GO; this phenomenon is generally attributed to a decrease in the average size of the sp² domain.

3.3. Effects of CNTs on the graphene membranes.

Both well-dispersed and poorly dispersed CNTs were obtained by adding and without adding BCPs, respectively, and were applied to the fabrication of graphene membranes. The effect of CNTs dispersion on the microstructure of the graphene membranes is shown in Fig. 4. Prepared with poorly dispersed CNTs, the surface of the composite graphene membrane is shown to be non-uniform. Both strong and poor CNTs enrichment regions are shown in Fig. 4a. Additionally, a slice of the CNTs blocks exist in the surface of composite graphene membrane (Fig. 4b), which may trigger strong defects. Conversely, the membrane surface is flat and defect-free due to the good CNTs dispersion, as shown in Fig. 4c, d. Well-dispersed 1D CNTs are buried in 2D graphene sheets and connect to form a uniform network (Fig. 4e, f). Consequently, mass transfer channels with continuous 3D nanostructure are created.

The effect of CNTs dispersion on the permeability and retention properties of rGO-CNTs hybrid membranes are shown in Table 1. The concentration of dyes was 50 ppm. The rGO-CNTs hybrid NF membranes derived from poor dispersed CNTs show larger fluxes and significantly worse retentions. However, the rGO-CNTs hybrid NF membranes derived from well-dispersed CNTs exhibit good retention performance for various dyes. By comparison, the flux of poorly dispersed membranes increased by nearly two-fold, and the rejection decreased by approximately half during the separation process of dyes with larger molecular weights, such as direct red 80, chlorazol fast pink, chlorazol black and titan yellow. Conversely, the poorly

Table 2 Effect of membrane thickness on the permeability and retention properties of rGO-CNTs hybrid membranes

Sample name		GM80	GM160	GM240	GM320	GM400
Thickness	d/nm	310	600	890	1100	1550
Pure water	$J_0/\text{L}\cdot\text{m}^{-2}\cdot\text{h}^{-1}\cdot\text{bar}^{-1}$	65	32	20	16	13
Direct Red 80	R/%	>99	>99	>99	>99	>99
Chlorazol Fast Pink	R/%	>99	>99	>99	>99	>99
Chlorazol Black	R/%	>99	>99	>99	>99	>99
Titan Yellow	R/%	98.5	>99	>99	>99	>99
Methyl Orange	R/%	90.2	97.3	97.8	98.1	98.2

dispersed membrane showed a lower retention for methyl orange due to its lower molecular weight. These effects may be due to the defects caused by the poor dispersion of the CNTs. It has been reported that the defects have a significant impact on the performance of NF.⁵¹ Additionally, after the test of pure water flux, the rGO-CNTs hybrid membrane was dried at 70 °C for 12 h to remove the residual water. Then, we measured the mass release ratio during the test of pure water flux. It was found that the hybrid membrane was stable and the mass release ratio was almost 0%, which even couldn't be detected by using one over ten-thousand analytical balance.

To further describe the effect of CNTs dispersion on the performance of graphene membranes that containing some concentration of BCPs, pure-water permeabilities were measured for various membranes with different components. All membranes were prepared with a thickness of approximately 600 nm. The pure-water permeability was found to be low for graphene membranes without CNTs but increased by nearly two orders of magnitude for those with CNTs (Fig. 5). Conversely, the pure-water permeability was found to not be strongly affected by the existence of BCPs in graphene

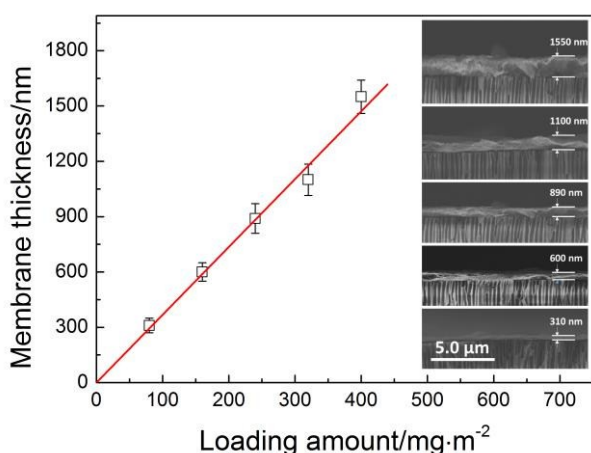


Fig. 6 Effect of load on the membrane thickness.

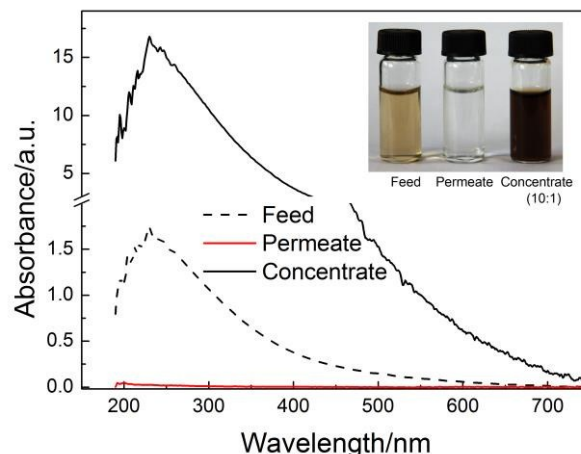


Fig. 7 Performance of rGO-CNTs hybrid NF membranes for removing humic acid from water.

membranes without CNTs. It can be inferred from these results that the addition of CNTs is a key strategy to improve the pure-water permeability of graphene membranes; this is likely caused by the fact that water transfer channels in the graphene membrane that were intercalated by well-dispersed carbon nanotubes are larger and shorter than those in a pure membrane. The effect of CNTs on the structure of the graphene membrane is shown in the inset of Fig. 5. Based on Darcy's law, a larger pore size and shorter pathway in this membrane decrease the transport resistance and increase the flux.

Effect of CNTs loadings on the performance was also studied (Table S1). All membranes were prepared with a thickness of approximately 600 nm. The concentration of dyes was 50 ppm. It could be found that increasing the nanochannels of the rGO-CNTs membrane by increasing the CNTs loadings can further improve the pure water permeability, but simultaneously give rise to the sacrifice of retention property if the lamellar structures of the hybrid membrane are destroyed by too many CNTs. The rGO-CNTs hybrid membrane with an optimised mass ratio $m(\text{rGO}):m(\text{CNTs})$ of 2:1 shown high permeability without sacrificing their retention properties.

A scratch test was also performed to analyze the strength and scratch resistance of the rGO-CNTs hybrid membrane (Fig. S8). The membrane showed a shorter scratch mark than the GO and rGO membranes; the bond between the AAO substrate and the rGO-CNTs hybrid membrane layer was thus sufficiently robust, mitigating any stripping phenomenon. Conversely, the membrane layer peeled off at the same displacement for the rGO membrane without CNTs, indicating the well-dispersed 1D CNTs could enhance the strength and scratch resistance of graphene membranes.

3.4. Effect of membrane thickness on the graphene membranes.

rGO-CNTs hybrid membranes with different thicknesses were created by controlling the total loading amount of graphene and CNTs. Fig. 6 shows that the membrane thickness increases linearly as the total loading amount of graphene and CNTs increase. Additionally, the top layer thickness was found to be

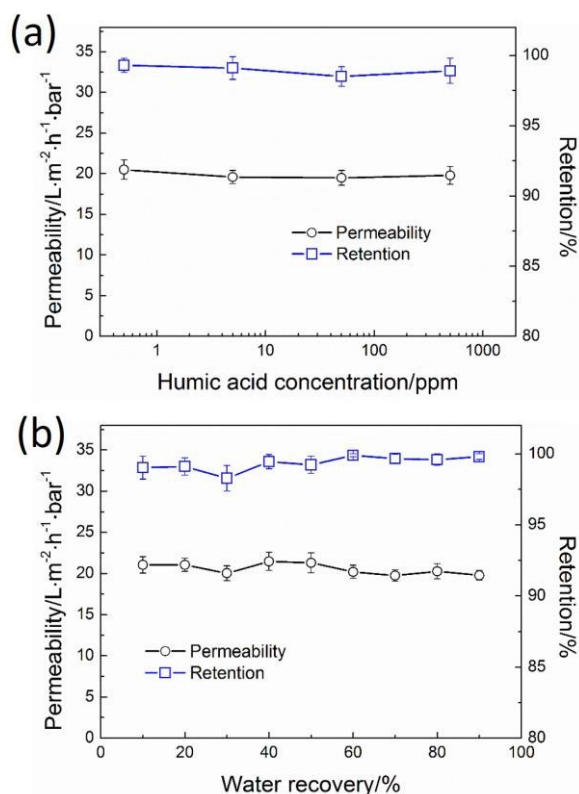


Fig. 8 (a) Effect of humic acid concentration in the feed on the performance of the rGO-CNT NF membranes. (b) Performance of the rGO-CNTs NF membranes at removing humic acid.

uniform, and the boundary of the top layer and the AAO substrate is easily identified.

The effect of membrane thickness on the permeability and retention properties of rGO-CNTs hybrid membranes are shown in Table 2. The rGO-CNTs hybrid membranes with the total loading amount of carbon materials from 80 to 400 $mg \cdot m^{-2}$ are denoted as GM80, GM160, GM240, GM320 and GM400, respectively. The pure-water flux is shown to decrease as the membrane thickness increases. All membranes with different thicknesses show good retention properties for direct red 80, chlorazol fast pink and chlorazol black. However, membrane GM80 exhibits the least retention for titan yellow and methyl orange; this result was likely due this membrane's thinner membrane thickness, which may increase the prevalence of defects in the membrane. For methyl orange, the retention is shown to be lower than the other dyes, which implies that methyl orange has a smaller molecular weight and size than the other dyes tested in this study. Overall, the optimized membrane thickness was selected to be 600 nm to obtain rGO-CNTs hybrid membranes with both a high flux and strong retention properties.

3.5. Performance of graphene NF membranes.

The as-prepared rGO-CNTs hybrid NF membranes (GM160) were used for drinking water purification. The average roughness of rGO-CNTs hybrid NF membrane was about 25 nm. It suggested that the surface of hybrid NF membrane was

smooth. The water contact angle of this hybrid NF membrane was about 40° which indicated the surface was hydrophilic. In addition to the dyes, the retentions of several modeled pollutants, such as small organic matters, nanoparticles, proteins and pesticides, in drinking water were also investigated.

Fulvic acid, which is a type of humic acid, is a primary organic pollutant in water and a major contributor to fouling of membranes, particularly the organic polymeric membranes.⁵² However, the removal of fulvic acid is difficult even via UF membranes due to their low molecular weight (550 ± 10 Da).⁵³ Conversely, the rGO-CNTs hybrid NF membranes exhibit high performances with regard to the rejection of fulvic acid (Fig. 7). The feed is shown to be yellow in color, but the permeate is clear and transparent. When the fulvic acid in the feed was increased in concentration by 10 times, the solution turned dark brown in color. These results clearly indicate that the humic acid has been nearly completely rejected by the rGO-CNTs hybrid NF membranes. Additionally, the comparison of the AAO substrate, the rGO-CNTs hybrid NF membrane and the CNTs membrane with regard to permeability and retention performance is shown in Fig. S9. The AAO substrate shows a high permeability of approximately 3800 and 2000 $L \cdot m^{-2} \cdot h^{-1} \cdot bar^{-1}$ for pure water and humic acid solution, respectively, and a low retention for humic acid. These results suggest that the retention properties for humic acid can be attributed to the graphene-based top layer; the AAO substrate simply acts as the support for the rGO-CNTs hybrid membrane and does not contribute to the rejection properties of the membrane. In addition, CNTs membrane prepared from well-dispersed CNTs also shows a high permeability of approximately 1950 and 1100 $L \cdot m^{-2} \cdot h^{-1} \cdot bar^{-1}$ for pure water and humic acid solution, respectively, and a low retention for humic acid. It indicates that the pure CNTs membrane has a larger pore size, which is out of the range of NF.

The effect of the humic acid concentration in the feed on the separation and retention properties for rGO-CNTs NF membranes is shown in Fig. 8a. The retention and permeability of the graphene NF membrane remain at stable and high levels as the humic acid concentration in the feed increases, indicating

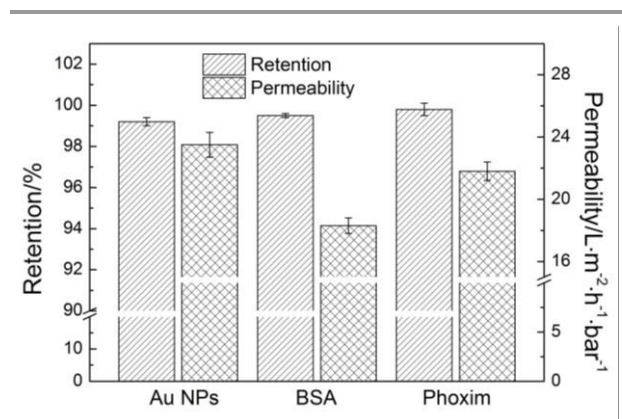


Fig. 9 Performance of rGO-CNTs NF membranes for the retention of Au nanoparticles, BSA and phoxim.

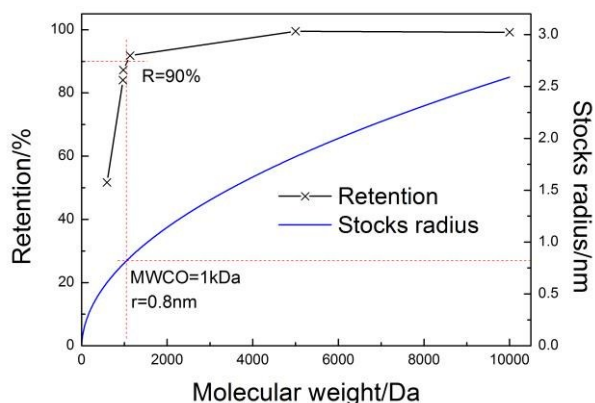


Fig. 10 Retention curve of various sugars for rGO-CNTs hybrid NF membrane.

that the rGO-CNTs NF membranes can effectively adapt to such conditions without sacrificing their high performance.

Additionally, the continuous concentration process for humic acid with an initial concentration of 50 ppm was investigated. The effect of the water recovery ratio on the performance of the rGO-CNTs NF membrane is shown in Fig. 8b. As the water recovery ratio increased from 0% to 90%, both the permeability and retention remained relatively unchanged. The effect of the concentration rate on the humic acid concentration in the feed was also investigated (Fig. S10); the humic acid concentration in the feed is shown to relate linearly with the concentration rate. Additionally, nearly all of the rejected humic acid remained in the feed solution rather than being adsorbed onto the membrane surface. There is thus clear evidence that rGO-CNTs NF membranes exhibit good resistance to the fouling of humic acid in water. It might be due to the smooth and hydrophilic membrane surface.

This continuous concentration process was repeated nine additional times. After each cycle, the NF membrane was washed with pure water until its permeability for pure water reached that of its new level (i.e., $30 \pm 1 \text{ L} \cdot \text{m}^{-2} \cdot \text{h}^{-1} \cdot \text{bar}^{-1}$). Fig. S11 shows that the graphene NF membrane exhibits stable performance for the retention of humic acid, and its permeability and retention properties remain strong and stable.

Au nanoparticles, BSA and phoxim were chosen as the modeled nanoparticles, protein and pesticide in drinking water, respectively. As shown in Fig. 9, the NF membrane shows good retention and high flux for Au nanoparticles, BSA and phoxim; the retention for Au nanoparticles, BSA and phoxim are as high as 99.2%, 99.5% and 99.8%, respectively. Additionally, the permeability of Au nanoparticles, BSA and phoxim increased up to $22\text{--}30 \text{ L} \cdot \text{m}^{-2} \cdot \text{h}^{-1} \cdot \text{bar}^{-1}$, which are markedly larger than those for graphene NF membranes that are reported in the literature.^{35, 54} The retention properties for sugars were also investigated and are shown Fig. S12. The retention curve was also calculated and is shown in Fig. 10; the retention is shown to increase as the molecular weight of the sugar increases. The MWCO was calculated to be equal to approximately 1 kDa, which corresponds to a stocks radius of approximately 0.8 nm. These high permeabilities and strong separation properties can

likely be attributed to the 3D mass transfer channels of graphene NF membrane that are constructed by combining the well-dispersed 1D carbon nanotubes and the single-atom-thick 2D graphene sheets.

The hybrid NF membranes were also applied to separate ions from drinking water. The retentions of hybrid NF membrane to four kinds of salt Na_2SO_4 , NaCl , MgSO_4 and MgCl_2 were tested at the concentration of 0.005 M under a pressure of 3 bar. The permeabilities of different salt solutions were similar and were as high as about $28 \text{ L} \cdot \text{m}^{-2} \cdot \text{h}^{-1} \cdot \text{bar}^{-1}$. A high rejection of Na_2SO_4 was achieved at about 84%. As shown in Fig. S13, retention of the divalent anion (SO_4^{2-}) was higher than those of the monovalent anion (Cl^-). It could be explained by Donnan effect, which is usually applied to explain the retention mechanism for charged NF membranes.⁵⁴ Such behaviour is typical for negatively charged NF membranes. In other words, the rGO-CNTs hybrid NF membranes are negatively charged due to the carboxylic groups at the edges and holes of rGO sheets. Moreover, the presence of counter-ions, which could bind part of the surface charge, may weaken the repulsive force, resulting in a higher retention for sodium salts (Na_2SO_4 and NaCl) than magnesium salts (MgSO_4 and MgCl_2). As a result, a retention (R) sequence of different salt solutions was obtained as $R(\text{Na}_2\text{SO}_4) > R(\text{NaCl}) > R(\text{MgSO}_4) > R(\text{MgCl}_2)$.

Conclusions

Graphene NF membranes that were intercalated with Carbon nanotubes were fabricated on porous ceramic microfiltration membranes using a facile vacuum-assisted filtration method. CNTs were dispersed effectively using F127 as a surfactant. The well-dispersed 1D carbon nanotubes were placed inside of 2D graphene sheets to form an uniform network. The good CNTs dispersion markedly effected the performance of the rGO-CNTs hybrid NF membranes. The optimized rGO-CNTs hybrid NF membranes were tested with drinking water treatment and exhibited high performances in terms of their retention efficiencies (i.e., primarily above 99%) and their permeabilities (i.e., as high as $20\text{--}30 \text{ L} \cdot \text{m}^{-2} \cdot \text{h}^{-1} \cdot \text{bar}^{-1}$) for the retention of nanoparticles, dyes, BSA, sugars and particularly humic acid. The results of this study thus demonstrate that rGO-CNTs hybrid NF membranes are promising for drinking water purification.

Acknowledgments

This study was financially supported by the National High Technical Research Program of China (2012AA03A606), the Project of Priority Academic Program Development of Jiangsu Higher Education Institutions (PAPD), the Graduate Research and Innovation Projects in Jiangsu Province (KYZZ15_0225), the Major Program of the Nature Science for Higher Education Institutions of Jiangsu Province (12KJA530001), and the Program for Changjiang Scholars and Innovative Research Team in University (IRT13070).

Notes and references

- 1 *Global risks 2015*, World Economic Forum, Geneva, 2015.
- 2 E. Drioli and L. Giorno, *Comprehensive membrane science and engineering*, Elsevier, Holland, 2010.
- 3 F. C. Kramer, R. Shang, S. G. J. Heijman, S. M. Scherrenberg, J. B. van Lier and L. C. Rietveld, *Sep. Purif. Technol.*, 2015, **147**, 329-336.
- 4 X. Da, J. Wen, Y. Lu, M. Qiu and Y. Fan, *Sep. Purif. Technol.*, 2015, **152**, 37-45.
- 5 J. Palmeri, J. Sandeaux, R. Sandeaux, X. Lefebvre, P. David, C. Guizard, P. Amblard, J. F. Diaz and B. Lamaze, *Desalination*, 2002, **147**, 231-236.
- 6 X. Lefebvre, J. Palmeri, J. Sandeaux, R. Sandeaux, P. David, B. Maleyre, C. Guizard, P. Amblard, J. F. Diaz and B. Lamaze, *Sep. Purif. Technol.*, 2003, **32**, 117-126.
- 7 C. Mazzoni, F. Orlandini and S. Bandini, *Desalination*, 2009, **240**, 227-235.
- 8 X. Chen, W. Zhang, Y. Lin, Y. Cai, M. Qiu and Y. Fan, *Microporous Mesoporous Mater.*, 2015, **214**, 195-203.
- 9 A. Maher, M. Sadeghi and A. Moheb, *Desalination*, 2014, **352**, 166-173.
- 10 B. Xi, X. Wang, W. Liu, X. Xia, D. Li, L. He, H. Wang, W. Sun, T. Yang and W. Tao, *Sep. Sci. Technol.*, 2014, **49**, 2642-2649.
- 11 A. Shahmansouri and C. Bellona, *Water Sci. Technol.*, 2015, **71**, 309-319.
- 12 W. Pang, N. Gao and S. Xia, *Desalination*, 2010, **250**, 553-556.
- 13 V. Uyak, I. Koyuncu, I. Oktem, M. Cakmakci and I. Toroz, *J. Hazard. Mater.*, 2008, **152**, 789-794.
- 14 K. Moons and B. Van der Bruggen, *Desalination*, 2006, **199**, 245-247.
- 15 G. Liu, W. Jin and N. Xu, *Chem. Soc. Rev.*, 2015, DOI: 10.1039/C4CS00423J.
- 16 V. Abetz, *Macromol. Rapid. Comm.*, 2015, **36**, 10-22.
- 17 P. S. Zhong, T. S. Chung, K. Jeyaseelan and A. Armugam, *J. Membr. Sci.*, 2012, **407**, 27-33.
- 18 J. Lee, H. R. Chae, Y. J. Won, K. Lee, C. H. Lee, H. H. Lee, I. C. Kim and J. m. Lee, *J. Membr. Sci.*, 2013, **448**, 223-230.
- 19 J. Park, D. Hong, D. Kim, K. E. Byun and S. Hong, *J. Phys. Chem. C*, 2014, **118**, 3742-3749.
- 20 S. P. Surwade, S. N. Smirnov, I. V. Vlasiouk, R. R. Unocic, G. M. Veith, S. Dai and S. M. Mahurin, *Nat. Nanotechnol.*, 2015, **10**, 459-464.
- 21 H. Huang, Z. Song, N. Wei, L. Shi, Y. Mao, Y. Ying, L. Sun, Z. Xu and X. Peng, *Nat. Commun.*, 2013, **4**, 2979-2987.
- 22 B. X. Mi, *Science*, 2014, **343**, 740-742.
- 23 R. K. Joshi, P. Carbone, F. C. Wang, V. G. Kravets, Y. Su, I. V. Grigorieva, H. A. Wu, A. K. Geim and R. R. Nair, *Science*, 2014, **343**, 752-754.
- 24 H. Li, Z. Song, X. Zhang, Y. Huang, S. Li, Y. Mao, H. J. Ploehn, Y. Bao and M. Yu, *Science*, 2013, **342**, 95-98.
- 25 H. W. Kim, H. W. Yoon, S. M. Yoon, B. M. Yoo, B. K. Ahn, Y. H. Cho, H. J. Shin, H. Yang, U. Paik, S. Kwon, J. Y. Choi and H. B. Park, *Science*, 2013, **342**, 91-95.
- 26 R. R. Nair, H. A. Wu, P. N. Jayaram, I. V. Grigorieva and A. K. Geim, *Science*, 2012, **335**, 442-444.
- 27 J. L. Achtyl, R. R. Unocic, L. Xu, Y. Cai, M. Raju, W. Zhang, R. L. Sacchi, I. V. Vlasiouk, P. F. Fulvio, P. Ganesh, D. J. Wesolowski, S. Dai, A. C. van Duin, M. Neurock and F. M. Geiger, *Nat. Commun.*, 2015, **6**, 6539-6544.
- 28 Q. Xu, H. Xu, J. Chen, Y. Lv, C. Dong and T. S. Sreeprasad, *Inorg. Chem. Front.*, 2015, **2**, 417-424.
- 29 X. Chen, G. Liu, H. Zhang and Y. Fan, *Chin. J. Chem. Eng.*, 2015, **23**, 1102-1109.
- 30 M. Hu and B. X. Mi, *Environ. Sci. Technol.*, 2013, **47**, 3715-3723.
- 31 W. S. Hung, C. H. Tsou, M. De Guzman, Q. F. An, Y. L. Liu, Y. M. Zhang, C. C. Hu, K. R. Lee and J. Y. Lai, *Chem. Mater.*, 2014, **26**, 2983-2990.
- 32 A. Nicolai, B. G. Sumpter and V. Meunier, *PCCP*, 2014, **16**, 8646-8654.
- 33 C. P. Athanasekou, S. Morales Torres, V. Likodimos, G. E. Romanos, L. M. Pastrana Martinez, P. Falaras, D. D. Dionysiou, J. L. Faria, J. L. Figueiredo and A. M. T. Silva, *Appl. Catal. B-Environ.*, 2014, **158**, 361-372.
- 34 W. Wang, E. Eftekhari, G. Zhu, X. Zhang, Z. Yan and Q. Li, *Chem. Commun.*, 2014, **50**, 13089-13092.
- 35 Y. Han, Y. Jiang and C. Gao, *ACS Appl. Mater. Inter.*, 2015, **7**, 8147-8155.
- 36 S. J. Gao, H. Qin, P. Liu and J. Jin, *J. Mater. Chem. A*, 2015, **3**, 6649-6654.
- 37 K. Goh, W. Jiang, H. E. Karahan, S. Zhai, L. Wei, D. Yu, A. G. Fane, R. Wang and Y. Chen, *Adv. Funct. Mater.*, 2015, **25**, 7348-7359.
- 38 J. Zou, L. Liu, H. Chen, S. I. Khondaker, R. D. McCullough, Q. Huo and L. Zhai, *Adv. Mater.*, 2008, **20**, 2055-2060.
- 39 E. E. Tkalya, M. Ghislandi, G. de With and C. E. Koning, *Curr. Opin. Colloid. In.*, 2012, **17**, 225-231.
- 40 X. Xin, G. Xu, T. Zhao, Y. Zhu, X. Shi, H. Gong and Z. Zhang, *J. Phys. Chem. C*, 2008, **112**, 16377-16384.
- 41 Z. Wang, Q. Liu, H. Zhu, H. Liu, Y. Chen and M. Yang, *Carbon*, 2007, **45**, 285-292.
- 42 L. Tian, M. J. Meziani, F. Lu, C. Y. Kong, L. Cao, T. J. Thorne and Y. P. Sun, *ACS Appl. Mater. Inter.*, 2010, **2**, 3217-3222.
- 43 V. Georgakilas, A. Demeslis, E. Ntararas, A. Kouloumpis, K. Dimos, D. Gournis, M. Kocman, M. Otyepka and R. Zboril, *Adv. Funct. Mater.*, 2015, **25**, 1481-1487.
- 44 D. He, L. Shen, X. Zhang, Y. Wang, N. Bao and H. H. Kung, *AIChE J.*, 2014, **60**, 2757-2764.
- 45 P. Puhlfürß, A. Voigt, R. Weber and M. Morbé, *J. Membr. Sci.*, 2000, **174**, 123-133.
- 46 T. Liu, G. Xu, J. Zhang, H. Zhang and J. Pang, *Colloid. Polym. Sci.*, 2013, **291**, 691-698.
- 47 R. Shvartzman-Cohen, M. Florent, D. Goldfarb, I. Szleifer and R. Yerushalmi-Rozen, *Langmuir*, 2008, **24**, 4625-4632.
- 48 M. Florent, R. Shvartzman Cohen, D. Goldfarb and R. Yerushalmi-Rozen, *Langmuir*, 2008, **24**, 3773-3779.
- 49 R. Ivanova, B. Lindman and P. Alexandridis, *Adv. Colloid Interface Sci.*, 2001, **89-90**, 351-382.
- 50 J. F. Shen, Y. Z. Hu, M. Shi, X. Lu, C. Qin, C. Li and M. X. Ye, *Chem. Mater.*, 2009, **21**, 3514-3520.
- 51 S. Zeidler, P. Puhlfürß, U. Kätzel and I. Voigt, *J. Membr. Sci.*, 2014, **470**, 421-430.
- 52 J. J. Song, Y. Huang, S.-W. Nam, M. Yu, J. Heo, N. Her, J. R. V. Flora and Y. Yoon, *Sep. Purif. Technol.*, 2015, **144**, 162-167.
- 53 Y. Wang, R. Mao, Q. Wang, Z. Yang, B. Gao and Y. Zhao, *Desalination*, 2012, **302**, 55-64.
- 54 Y. Han, Z. Xu and C. Gao, *Adv. Funct. Mater.*, 2013, **23**, 3693-3700.